Supplementary Information

N-type graphene induced by dissociative H_2 adsorption at room temperature

Byung Hoon Kim[1], Sung Ju Hong[2], Seung Jae Baek[2], Hu Young Jeong[3], Noejung Park[1], Muyoung Lee[1], Sang Wook Lee[4], Min Park[2], Seung Wan Chu[2], Hyeon Suk Shin[1], Jeongmin Lim[1], Jeong Chul Lee[5], Yongseok Jun[1,*], Yung Woo Park[2,*]

[1]*Interdisciplinary School of Green Energy, KIER-UNIST Center for Energy, Ulsan National Institute of Science and Technology (UNIST), Ulsan 689-798, Republic of Korea*

[2]*Department of Physics and Astronomy, and Department of Nano Science and Technology, Seoul National University, Seoul 151-747, Republic of Korea*

[3]*UNIST Central Research Facility and School of Mechanical and Advanced Materials Engineering, Ulsan National Institute of Science and Technology (UNIST), Ulsan 689-798, Republic of Korea*

[4]*Division of Quantum Phases and Devices, School of Physics, Konkuk University, Seoul 143-701, Republic of Korea*

[5]*KIER-UNIST Advanced Center for Energy, Korea Institute of Energy Research, Daejeon, 305-343, Republic of Korea*

Experimental details

Measurement system for electrical transport in high H_2 pressure conditions.

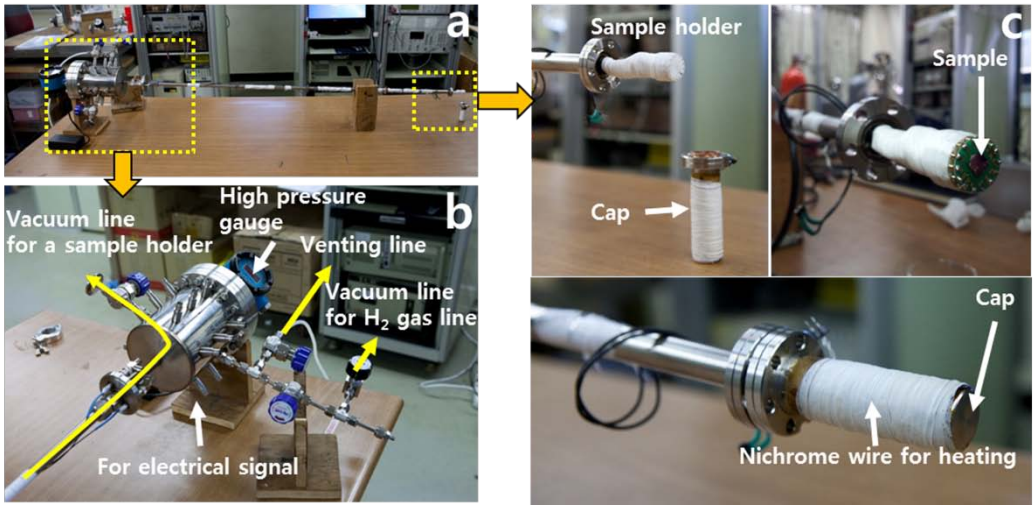

Figure S1. Probe for cryostat and high H_2 pressure. a, Full-lengh photograph of the probe **b,** Head of the probe consisted of two vacuum lines for a sample holder and H_2 gas line, venting line, high pressure gauge, and BNC type coaxial connector to sense an electrical signal. **c,** The sample holder is composed of a cap with nichrome wire for heating, Cu gasket, and chip holder made of Teflon.

Graphenes obtained by chemical vapor deposition (CVD) process.

Graphene on Cu foil was synthesized with some modifications of the method reported by X. Li *et al.*[S1] The foil was cut into 2 cm × 2 cm and pressed flat between two slide glasses and loaded into a 2 inch cylindrical alumina furnace. Before increasing the temperature, the chamber was evacuated and purged by argon gas to remove any oxygen and H_2O interrupting growth. Approaching 1050 ºC, annealing was carried out in argon 200 sccm and hydrogen 100 sccm with an atmospheric base pressure. Here, hydrogen gas is essential to remove the natural oxide layer and contaminations. In the growth process, methane and argon were flown through without hydrogen gas. After growth, the cooling procedure was performed by argon

gas. The graphene film was coated with Poly (methyl methacrylate) (PMMA) 950 K A4 (Microchem) and put into a copper etchant (Alfa aesar, stock # 44583) mixed $FeCl_3$ (25-30%), HCl (1-5%) and water (Balance) solution. 3~6 hours later, the Cu foil was sufficiently removed. Subsquently, rinsed in deionized (DI) water. Finally, the film was transferred onto a target substrate, dried for 1 day naturally, and the PMMA was removed by acetone and rinsed by a (IPA) solution[S2].

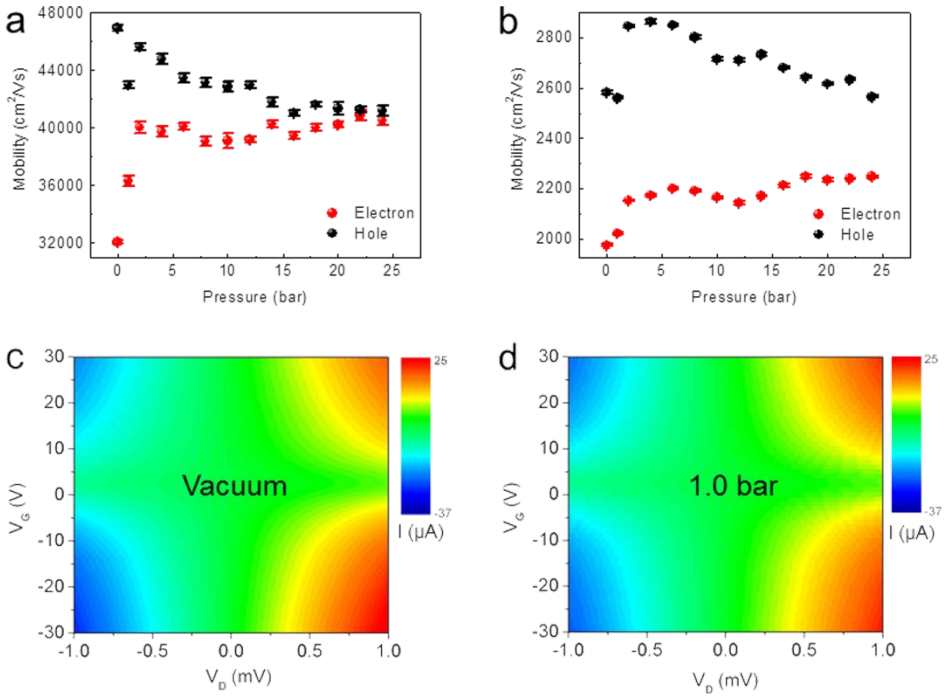

Figure S2. Electrical transport property of graphene a, and **b,** are the mobility of SLG and BLG, respectively. The mobility of MLG could not be obtained due to a narrow linear region in conductivity. *I-V* characteristics as a function of V_G for SLG in **c,** vacuum and **d,** 1.0 bar of H_2 pressure.

Figure S2 a and b show that electron and hole mobility (μ_e and μ_h, respectively) of SLG and BLG were obtained by $\mu = 1/C_g(d\sigma/dV_G)$, here C_g has a capacitance per unit area of 300 nm SiO_2 (1.15×10^{-2} μF/cm^2). In a vacuum μ_e and μ_h of SLG are 32,000 and 46,900 cm^2/V·s, respectively. In the case of BLG, μ_e and μ_h are respectively 1,970 and 2,580 cm^2/V·s. As H_2 pressure increases, we observed that μ_e increases but μ_h decreases. This behaviour is attributed to *n*-type doping due to H_2 exposure. We also obtained V_G-dependent *I-V* curve. Upon H_2 exposure, electrical currents enhances in $V_G > V_{CNP}$ regions. On the contrary, the current is suppressed in $V_G < V_{CNP}$ regions. It reveals the *n*-doping effect due to H_2 exposure. The same behaviour was also observed in BLG and MLG.

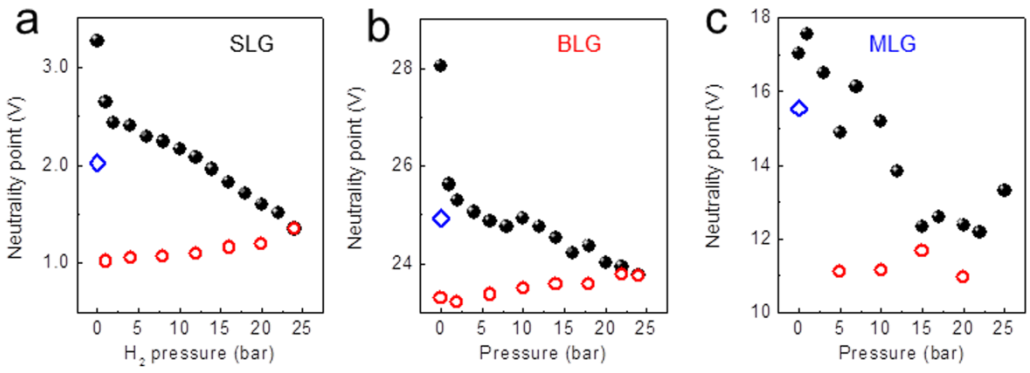

Figure S3. Dissociative H_2 adsorption. **a, b,** and **c,** show the variation of CNP for SLG, BLG, and MLG, respectively. H_2 exposure and release process are described by spheres and circles. The CNP does not turn back to the original value obtained before H_2 exposure (blue diamond).

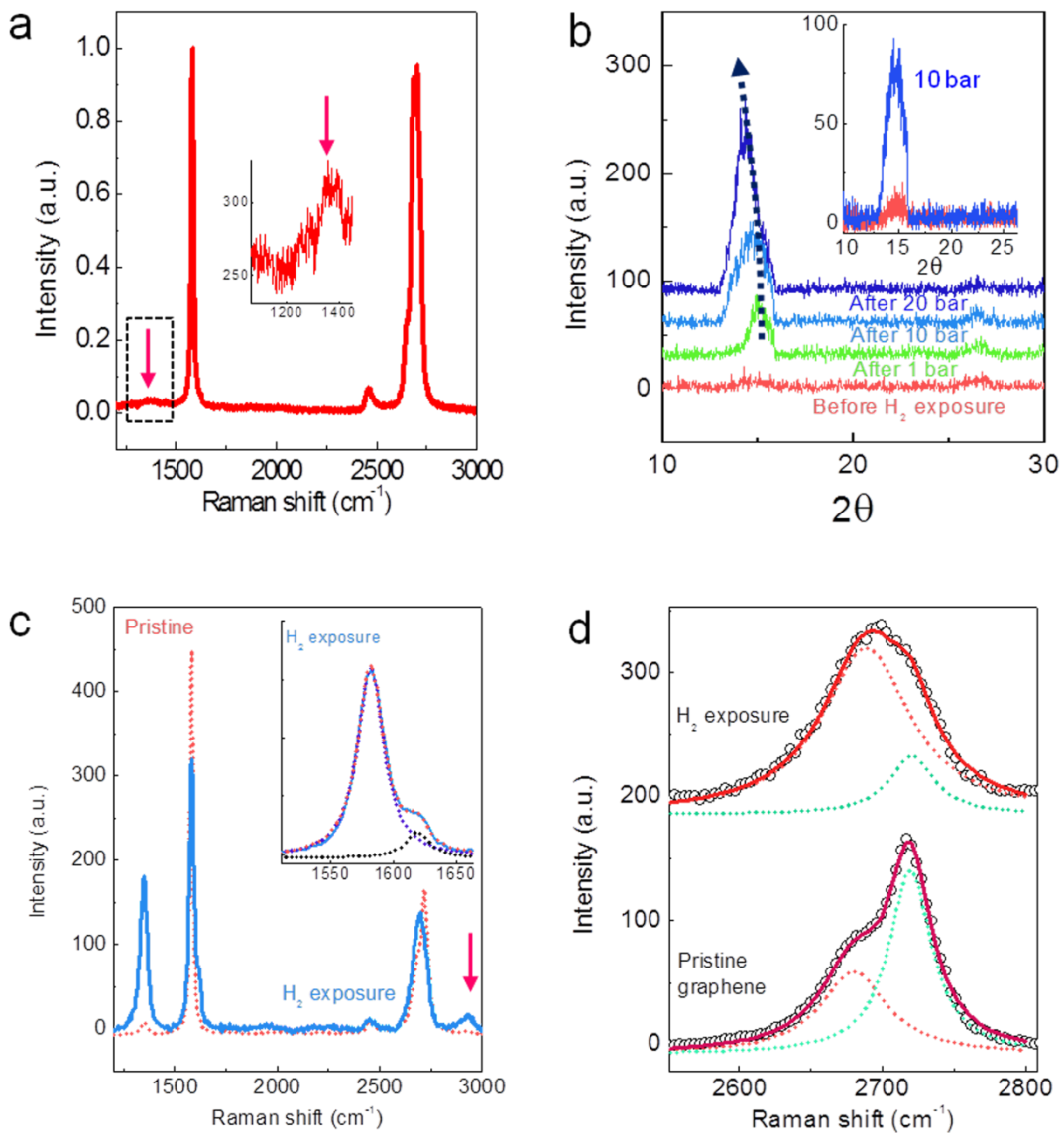

Figure S4. The structural modulation of graphene after H_2 exposure. **a,** Raman spectroscopy for BLG. The inset shows the magnified plot of *D* band. **b,** X-ray diffraction patterns for CVD graphene transferred on SiO_2/Si. The inset depicts graphene transferred on SiN. **c,** The change of Raman spectrum of CVD graphene upon H_2 exposure. The arrow indicates C–H stretching mode at 2932 cm^{-1}. The inset shows the development of *D′* peak after H_2 exposure. **d,** *2D* band for CVD graphene before (lower) and after H_2 exposure (upper).

Figure S4a shows the Raman spectrum for BLG after H_2 exposure, where a small *D* peak develops. BLG is much less reactive compared with SLG and MLG as reported in the literature[S3]. To confirm the enlargement of the interlayer distance of graphene and to exclude the effect of H_2 dissociation on metal electrodes, we synthesized multilayer graphene by CVD method on Cu foil and transferred it onto a SiO_2/Si substrate (Fig. S4b). Before H_2 exposure, very small peaks near $2\theta = 15.8$ º (5.61 Å) and 26.5 º (3.36 Å) can be seen. The small peaks are attributed to the few layer graphene grown by CVD. Upon H_2 exposure, even 1 bar of H_2, the peak near $2\theta = 15.8$º (5.61 Å) becomes larger and shifts to a lower angle: 5.99 Å at 10 bars and 6.16 Å at 20 bars. The interlayer distance of few-layered graphene increases depending on H_2 pressure. The same behaviour was observed in CVD graphene transferred on a SiN substrate as shown in the inset.

The increase of *D* peak but decrease of *G* peak in Raman spectra for CVD graphene were significant compared with those of the graphenes mechanically exfoliated (Fig. S4c). After H_2 exposure, *G* peak is not only blue-shifted from 1518.2 to 1582.5 cm^{-1} but broadened from 16.3 to 25.0 cm^{-1} in full width at half maximum. In addition, *D′* peak and C–H stretching mode were also observed at 1619 (the inset) and 2932 cm^{-1} (arrow), respectively, in CVD graphene. This indicates breaking of the translational symmetry of graphene due to the formation of C-H sp^3 bonds[S4]. The *2D* band near 2700 cm^{-1} in MLG shows that 2-D property of graphite increases but 3-D graphitic structure decreases indicating the absence of a stacking order due to dissociative adsorption of H_2 on graphene like mechanically exfoliated graphene.

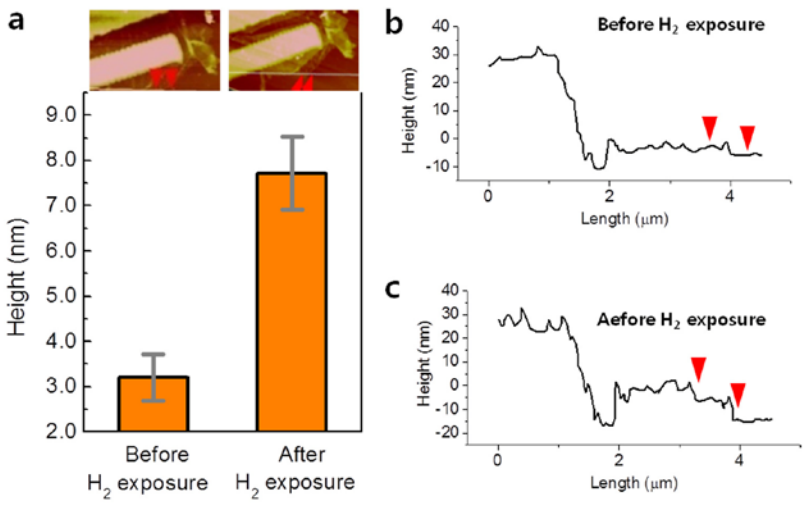

Figure S5. a, The thickness variation obtained by the AFM study shows an almost doubleincrease of the interlayer distance of MLG after H_2 exposure (right image). AFM line profiles of MLG **b,** before and **c,** after H_2 exposure. AFM topography in Fig. b is rotated to compare that in Fig. a. The width of electrode is 1.0 μm.

The AFM study was performed to observe the interplanar distance. We observed the increase in the thickness of MLG from 3.2 ± 0.52 nm to 7.2 ± 0.82 nm after H_2 exposure (Fig. S5a.) Figs. S5b. and S5c show one of the line profiles for MLG before and after H_2 exposure, respectively. From the topography one can easily find the thickness becomes larger after H_2 exposure because the bright region in the topography indicates the higher thickness. In the figure, the thickness of MLG changes from 3.890 nm to 7.587 nm due to H_2 exposure. The average thicknesses obtained from ten profiles near one area (near the red arrowhead in the Fig. S5.) are 3.2 ± 0.52 nm and 7.2 ± 0.82 nm respectively as mentioned in the main text. Here we focus on the value 3.2 ± 0.52 nm before H_2 exposure. It has been reported that the thickness of a single-layer graphene on SiO_2 substrate is over 1.0 nm due to interfacial interaction between graphene and SiO_2[S5]. Therefore the thickness of the MLG is roughly about 2.2 nm which corresponds to six layers of graphene.

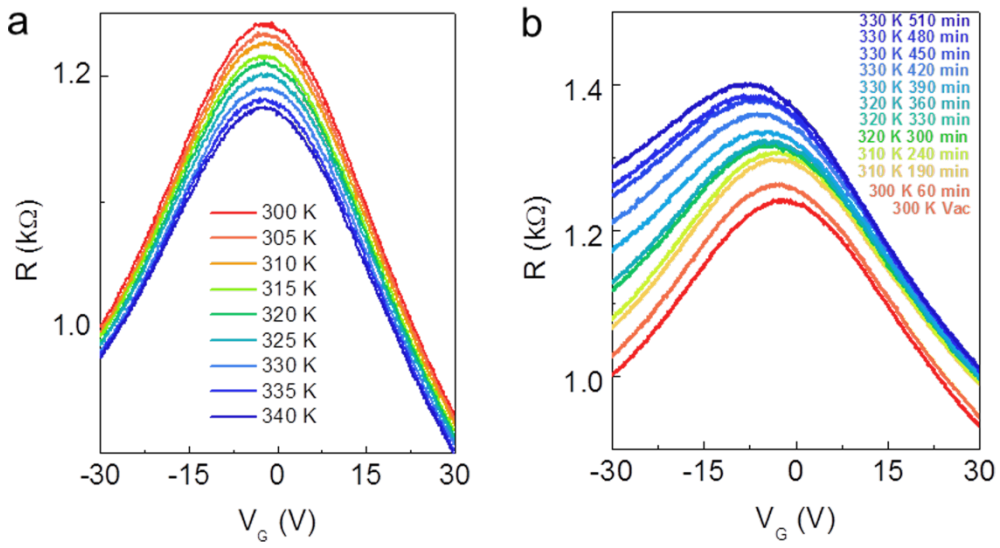

Figure S6. a, V_G-dependent R for MLG as a function of temperature. As temperature increases, R decreases. It results from the gap-opening of MLG. No shift of CNP was observed. **b,** V_G-dependent R as a function of temperature and exposure time for MLG in 10 bar of H_2 pressure. Longer exposure time enhances *n*-doping effect.

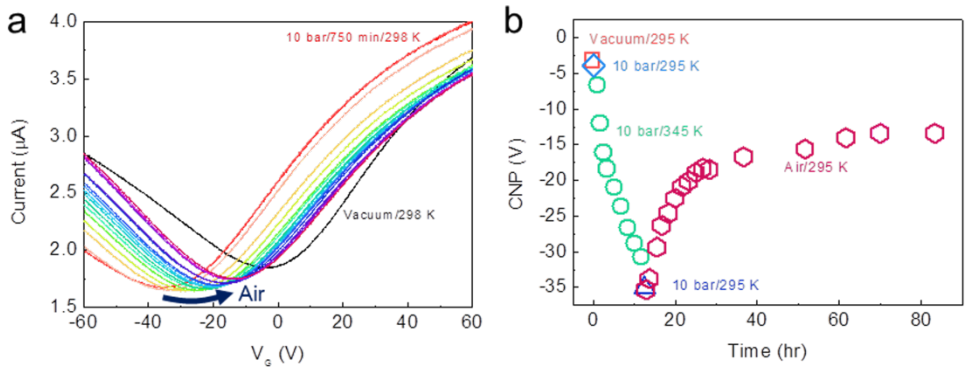

Figure S7. a, V_G-dependent current variation and **b,** CNP variation for MLG in air after 10 bar of H_2 exposure at 345 K.

To investigate air stability of *n*-type behaviour, 10 bars of H_2 pressure was applied to a MLG at 295 K and then the temperature was increased up to 345 K. After waiting sufficient time (~ 16 hrs), the temperature was decreased down to 295 K. Finally the MLG was exposed in air. CNP at -35 V due to dissociative H_2 adsorption shifts toward a positive V_G region. However, the variation of CNP was reduced, and finally CNP is saturated for nearly 60 hrs. This reveals that the graphene is hydrogenated and the air stable *n*-type graphene can be achieved by molecular hydrogen exposure.

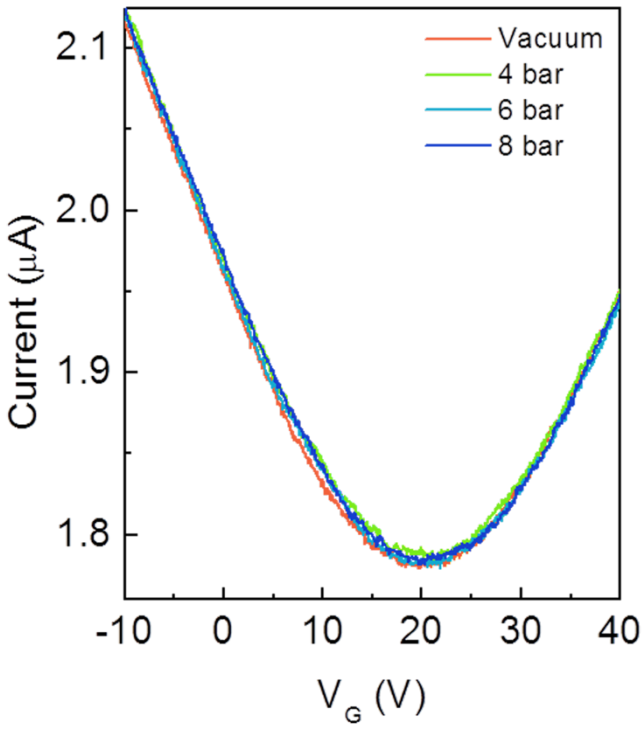

Figure S8. V_G-dependent current variation for MLG as a function of He pressure.

We consider several effects such as pressure, interaction SiO_2 with H_2 molecules, removal effect of surface residues, and H_2 dissociation due to Ti adhesion layer. First, to exclude a pressure effect, we performed the same experiment with He gas. No shift of CNP was observed in the V_G-dependent R as a function of He pressure (Fig. S8), indicating that the structural distortion caused by pressure cannot be the reason for the *n*-doping. Second, it has been reported that H_2 is dissociated and O vacancy site of SiO_2 captures a hole[S6]. However, it cannot explain the different doping effect for three kinds of graphenes (SLG, BLG, and MLG) and the relation between the number of graphene layers and ΔV_{CNP}. Third, the removal effect of surface admolecules can be ruled out with the same reason.

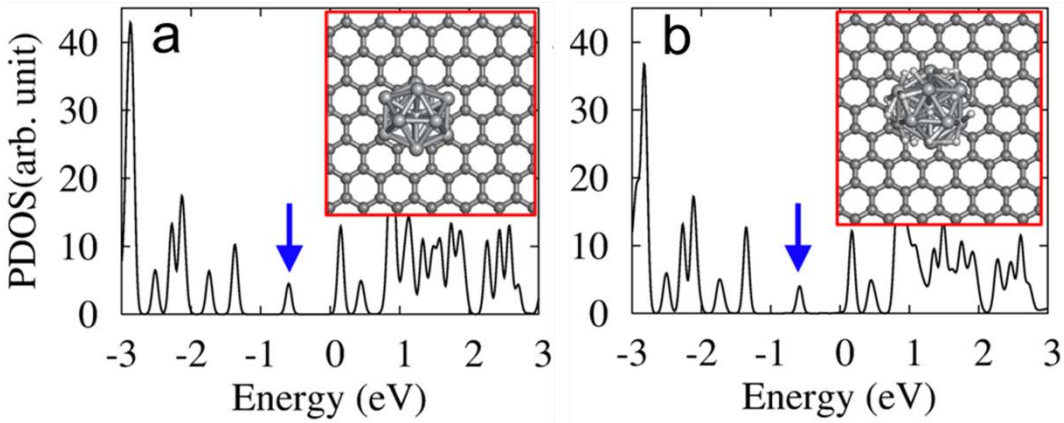

Figure S9. PDOS for the graphene when there is adsorbed **a,** Ti and **b,** hydrogenated Ti nanparticles. The inset shows the optimized geometries. Large-sized and medium-sized dark gray balls represent Ti and C atoms. Small bright gray balls represent H atoms. Downward arrows indicate the Dirac point. The energies in the horizontal axis are with respect to the Fermi level of each case.

Finally, it is possible that Ti adhesion layer of electrodes behaves as a hydrogen catalyst such as Ti-decorated Mg[S7, S8]. To investigate the effect of Ti adhesion layer, we performed first-principles density functional calculations for the accumulated hydrogen on the Ti electrode metal surface. For computations, we used the Vienna *ab initio* simulation package (VASP) to calculate the ground state of many electrons system in the framework of density functional theory[S9-S11]. A plane-wave basis set with an energy cut-off of 400 eV and PBE-type gradient-corrected exchange-correlation potential were employed[S12]. In our model geometries, a Ti nanoparticle was placed on graphene: One Ti_{13} in the shape of icosahedron in the triangular supercell of 98 carbon atoms. For the model of hydrogen accumulated Ti surface, we optimized the Ti nanoparticle with 20 hydrogen atoms adsorbed on the centre of 20 triangular faces on the icosahedron. Figures S9a and b show the partial density of electronic states (PDOS) for carbon atoms in the Ti and hydrogenated Ti nanoparticle-adsorbed graphene, respectively. As expected from the feature of small work function of Ti, the Fermi

level sits higher position than the Dirac point of graphene for the pure graphene. In the case of hydrogenated Ti, the Fermi level position is almost the same as that of bare Ti_{13}. Even though the hydrogenated Ti surface can have a smaller work function than a pure Ti surface, it is expected that such variation in the work function has negligible effect on the Fermi level alignment at the interface with graphene. This calculation reveals that Ti adhesion layer cannot explain the *n*-type doping on graphene.

References

S1. Li, X. *et al*. Large-area synthesis of high-quality and uniform graphene films on copper foils. *Science* **324,** 1312-1314 (2009).

S2. Regan, W. *et al*. A direct transfer of layer-area graphene. *Appl. Phys. Lett*. **96,** 113102 (2010).

S3. Ryu, S. *et al*. Reversible basal plane hydrogenation of graphene. *Nano Lett*. **8,** 4597-4602 (2008).

S4. Elias, D. C. *et al*. Control of graphene's properties by reversible hydrogenation: evidence for graphane. *Science* **323,** 610-613 (2009).

S5. Akcöltekin, S., Kharrazi, M. E., Köhler, B., Lorke, A. & Schleberger, M. Graphene on insulating crystalline substrates. *Nanotechnology* **20,** 155601 (2009).

S6. Tuttle, B. R., Hughart, D. R., Schrimpf, R. D., Fleetwood, D. M. & Pantelides, S. T. Defect interactions of H_2 in SiO_2: Implications for ELDRS and latent interface trap buildup. *IEEE Trans. Nucl. Sci*. **57,** 3046-3053 (2010).

S7. Du, A. J., Smith, S. C., Yao, X. D. & Lu, G. Q. The role of Ti as a catalyst for the dissociation of hydrogen on a Mg(0001) surface. *J. Phys. Chem. B* **109,** 18037-18041 (2005).

S8. Pozzo, M., Alfè, D., Amieiro, A., French, S. & Pratt, A. Hydrogen dissociation and diffusion on Ni- and Ti-doped Mg(0001) surfaces. *J. Chem. Phys*. **128,** 094703 (2008).

S9. Hohenberg, P. & Kohn, W. Inhomogeneous electron gas. *Phys. Rev.* **136,** B864-B871 (1964).

S10. Kresse, G. & Furthmüller, J. Efficient iterative schemes for ab initio total-energy calculations using a plane-wave basis set. *Phys. Rev. B* **54,** 11169-11186 (1996).

S11. Kresse, G. & Furthmüller, J. Efficiency of ab-initio total energy calculations for metals and semiconductors using a plane-wave basis set. *Comput. Mater. Sci*. **6,** 15-50 (1996).

S12. Perdew, J. P., Burke, K. & Ernzerhof, M. Generalized gradient approximation made simple. *Phys. Rev. Lett*. **77,** 3865-3868 (1996).